ORIGINAL PAPER

Linking microvascular collapse to tissue hypoxia in a multiscale model of pressure ulcer initiation

Vivek D. Sree[1] · Manuel K. Rausch[2] · Adrian B. Tepole[1,3]

Abstract

Pressure ulcers are devastating injuries that disproportionately affect the older adult population. The initiating factor of pressure ulcers is local ischemia, or lack of perfusion at the microvascular level, following tissue compression against bony prominences. In turn, lack of blood flow leads to a drop in oxygen concentration, i.e, hypoxia, that ultimately leads to cell death, tissue necrosis, and disruption of tissue continuity. Despite our qualitative understanding of the initiating mechanisms of pressure ulcers, we are lacking quantitative knowledge of the relationship between applied pressure, skin mechanical properties as well as structure, and tissue hypoxia. This gap in our understanding is, at least in part, due to the limitations of current imaging technologies that cannot simultaneously image the microvascular architecture, while quantifying tissue deformation. We overcome this limitation in our work by combining realistic microvascular geometries with appropriate mechanical constitutive models into a microscale finite element model of the skin. By solving boundary value problems on a representative volume element via the finite element method, we can predict blood volume fractions in response to physiological skin loading conditions (i.e., shear and compression). We then use blood volume fraction as a homogenized variable to couple tissue-level skin mechanics to an oxygen diffusion model. With our model, we find that moderate levels of pressure applied to the outer skin surface lead to oxygen concentration contours indicative of tissue hypoxia. For instance, we show that applying a pressure of 60 kPa at the skin surface leads to a decrease in oxygen partial pressure from a physiological value of 65 mmHg to a hypoxic level of 31 mmHg. Additionally, we explore the sensitivity of local oxygen concentration to skin thickness and tissue stiffness, two age-related skin parameters. We find that, for a given pressure, oxygen concentration decreases with decreasing skin thickness and skin stiffness. Future work will include rigorous calibration and validation of this model, which may render our work an important tool toward developing better prevention and treatment tools for pressure ulcers specifically targeted toward the older adult patient population.

Keywords Skin mechanics · Microvasculature mechanics · Oxygen perfusion · Finite element analysis · Multiscale model · Skin aging

✉ Adrian B. Tepole
abuganza@purdue.edu

1 Mechanical Engineering, Purdue University, West Lafayette, IN, USA

2 Aerospace and Engineering Mechanics, The University of Texas at Austin, Austin, TX, USA

3 Weldon School of Biomedical Engineering, Purdue University, West Lafayette, IN, USA

1 Introduction

Pressure ulcers are a serious medical condition, affecting more than 3 million individuals annually in the USA and leading to healthcare costs of approximately 16 billion dollars every year (Lyder and Ayello 2008). Pressure ulcers occur predominantly among the older adult population. In fact, between 7.3 and 23% of adults in nursing homes in Europe and the USA are affected by pressure ulcers (Demarré et al. 2015). It is now indisputable that a primary mechanism of pressure ulcer initiation is ischemia, or lack of blood perfusion. Ischemia leads to low oxygen concentration in the tissue, or hypoxia, triggering a cascade of inflammatory signals that culminate in ulceration (Kosiak

1961; Gawlitta et al. 2007; Liao et al. 2013; Coleman et al. 2014; Sree et al. 2019). However, despite this knowledge, prevention of pressure ulcers remains extremely challenging (Dealey et al. 2015). One reason for the difficulty in assessing pressure ulcer risk for an individual is that a quantitative connection between applied pressure, skin mechanical properties and anatomy, and tissue hypoxia has been minimally explored.

Technologies such as laser Doppler flowmetry enable clinicians to monitor skin perfusion and detect hypoxic levels that could lead to ulceration. However, these tools are uneconomical and thus not a viable option for the general population (Timar-Banu et al. 2001). Moreover, they provide an average measurement of oxygen concentration across the entire tissue thickness and offer no detail about the underlying mechanisms of pressure-driven ischemia (Manorama et al. 2010; Peirce et al. 2000; Colin and Saumet 1996). From investigation of the skin microvasculature, we have gained detailed knowledge of the vascular tree irrigating the skin (Braverman 1989; Braverman et al. 1990; Cevc and Vierl 2007). Yet, in vivo imaging and characterization of microvascular collapse as tissue deforms remains out of reach. Our knowledge of skin mechanical properties has also improved significantly in recent years, both through traditional ex vivo tests (Gerhardt et al. 2012) and novel noninvasive in vivo tests (Müller et al. 2018; Sadler et al. 2018). Unfortunately, knowledge of an individual's skin mechanical behavior alone is also insufficient to anticipate the levels of perfusion inside the skin in response to applied pressure.

High-fidelity computational models of soft tissue deformation and perfusion with realistic geometries and material properties can fill the gap in the current available imaging technologies. Computational models of skin mechanics have already permeated into the field of reconstructive surgery because of the importance of stress on wound healing (Mitchell et al. 2015; Tepole 2017; Lee et al. 2019). Skin, like most connective soft tissues, shows remarkable mechanical behavior (Kumaraswamy et al. 2017). It behaves as a nearly incompressible solid in timescales in the order of seconds, but shows stress relaxation and compressibility in the timescales going from minutes to hours (Lokshin and Lanir 2009; Weickenmeier et al. 2015; Limbert 2017). The mechanical behavior of skin in the short timescales has been modeled extensively within a hyperelastic framework (Lee et al. 2018; Jor et al. 2013). Multiphasic formulations accounting for interstitial fluid have been employed, although to a lesser extent, to model the stress relaxation in the longer timescales (Oomens et al. 1987). Computational modeling of blood flow in the microvasculature has received some attention (Vankan et al. 1997), but these efforts have not accounted for the mechanical behavior of the skin and the link to the deformation and collapse of the vasculature. In fact, few computational studies have been carried out in

the context of pressure ulcer formation accounting for the vasculature (Linder-Ganz and Gefen 2007; Shilo and Gefen 2012). While these efforts have been an important step toward a better understanding of pressure-driven ischemia, they have been limited to simplified, two-dimensional geometries. Additionally, these investigations focused on the mechanical response of skin and not on the link to hypoxia, which is the indisputable initiator of pressure ulcers. Therefore, there is a lack of models that explicitly consider the microstructure of the skin including the microvasculature and how mechanical deformation can alter blood perfusion leading to hypoxia.

1.1 Anatomy and microvasculature of human skin

Human skin is organized in multiple layers with different mechanical and biological properties (Hendriks et al. 2006; Pailler-Mattei et al. 2008). The outermost layer of the skin is called epidermis and is primarily comprised of keratinocytes. The epidermis in itself is subdivided into two general sublayers. The outermost sublayer of the epidermis is called stratum corneum and is formed by dead keratinocytes (Liu et al. 2016). The second sublayer is denoted viable epidermis, providing a niche for the living epidermal cells. The stratum corneum is formed as keratinocytes terminally differentiate within the viable epidermis and move up to the outer surface (Shimizu 2007). The epidermis is avascular, and a significant fraction of oxygen supply to the outer layers is due to diffusive uptake from the surrounding air (Stücker et al. 2002). Additional oxygen and nutrients for the epidermis are obtained through diffusion from the dermis, which is the layer of skin immediately below the epidermis (Shimizu 2007). The dermis is comprised of stiff collagen fibers and acts as the primary load-bearing member of human skin (Jor et al. 2013; Groves et al. 2013). It is also much thicker than the epidermis. The dermis can be further subclassified into three sublayers: the papillary dermis attached to the epidermis, a subpapillary, intermediate layer, and the reticular layer, connecting the skin to the underlying fat and muscle (Crichton et al. 2011).

Microvasculature in human skin mostly resides in the dermis and forms two distinct horizontal plexuses. The lower plexus is formed by perforating vessels from subcutaneous tissue that enter the reticular dermis. This layer is connected to an upper plexus through arterioles and venules ascending and descending, respectively, to and from the skin surface. These vessels undergo multiple subdivisions along their upward path, forming the upper horizontal plexus which also contains the capillary loops connecting the venules and arterioles inside the papillary dermis (Braverman et al. 1990; Braverman 1989). Braverman et al. have characterized the anatomy of these vessels by spatially reconstructing optical microscope images 1 μm thick sections of skin biopsies.
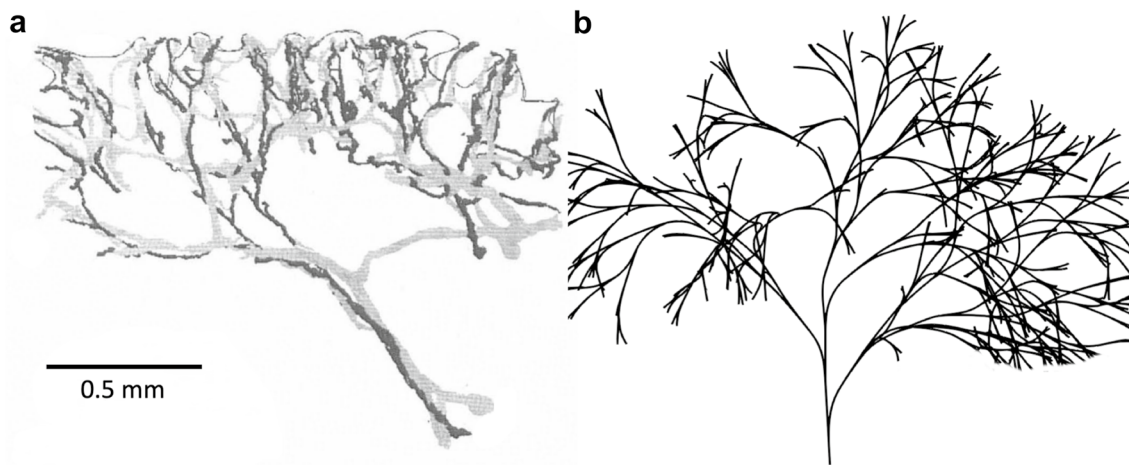
Fig. 1 Skin microvascular geometry. **a** Reconstructed image of the skin microvasculature from slices of a skin biopsy using optical microscopy reproduced with permission from Braverman et al. (1990). Skin is comprised of two horizontal plexuses that form a fractal tree structure. **b** Our fractal generating algorithm leads to realistic microvascular geometries

Figure 1a shows the structure of blood vessels in the skin as reported in their work (Braverman et al. 1990; Braverman 1989). These and other studies have shown that the vasculature structure in the skin is fractal in nature (Cevc and Vierl 2007; Gould et al. 2011). Indeed, fractals are a recurring pattern in some biological structures, such as vascular networks in most tissues including the skin (Hahn et al. 2005; Mandelbrot 1985), the Purkinje networks in the human heart (Goldberger et al. 1985), and the airways of the lungs (Tawhai et al. 2000). Cevc and Vierl (2007), for instance, have measured the change in vessel number, diameter, and length as the vascular tree undergoes multiple bifurcations along the skin thickness.

1.2 Linking vascular collapse to tissue hypoxia in aging skin

In this manuscript, we show that given existing knowledge of the detailed skin microvascular geometry and skin mechanical properties (Braverman 1989; Cevc and Vierl 2007), we are able to create a realistic multiscale model of oxygen perfusion. A microscale finite element model of a representative volume element (RVE) captures the intricate microvascular geometry in three dimensions and how it collapses under applied loads. The change in blood volume fraction predicted by the RVE model is then used as a homogenized variable at a tissue-level skin mechanics and oxygen diffusion model. Our study therefore crucially advances our current understanding of pressure ulcer initiation by connecting the mechanical behavior of skin, microvascular anatomy, and oxygen diffusion processes at multiple scales.

Aging induces changes in the mechanical properties and structure (e.g., thickness of different layers) of skin tissues (Daly and Odland 1979; Tonge et al. 2013; Krueger et al.

2011). However, it remains unclear how these changes potentially impact susceptibility to ischemia and could thus explain, at least in part, the increased risk of pressure ulcer formation in older adults. For instance, noninvasive suction tests on a large number of human subjects suggested that aging skin shows greater creep; i.e., the skin shows more extensibility after it has been loaded to the same pressure and duration of time (Luebberding et al. 2014). Animal models have also been used to characterize aging skin in detail. Experiments on mice have also shown a shift toward larger strains of the classical J-shaped stress-strain response of skin (Lynch et al. 2017). Our computational model allows us to investigate the change in skin mechanical behavior with aging in order to dissect the influence of tissue stiffness on the spatial distribution of tissue hypoxia under applied loads. Aging skin is also characterized by a decrease in thickness of the dermis, the load-bearing layer of skin (Leveque et al. 1984). Once again, it remains unknown how sensitive the oxygen concentration profile is to this change in skin structure. Here, we employ our computational model to investigate questions related to the mechanics of ischemia and how they may be affected by aging.

Pressure ulcers in the older adult population are associated with other factors not considered here, such as an increased inflammation response (Moor et al. 2014), lack of tissue regeneration ability (Park et al. 2009; Ashcroft et al. 1997), and behavioral factors such as a sedentary lifestyle (Allman et al. 1995). Mechanical damage and reperfusion injury are also important mechanisms in the subsequent stages of ulcer progression (Loerakker et al. 2010, 2011). Nevertheless, the current paradigm of pressure ulcer initiation suggests ischemia due to blood vessel deformation and associated hypoxia as the initiating mechanism (Coleman et al. 2014). Therefore, a better understanding of this event

is essential to improve prevention, diagnosis, and treatment of pressure ulcers.

2 Methods

2.1 Creation of microvascular trees

We generate fractal trees with the same characteristics as the skin's microvasculature (Fig. 1b) and use these geometries in a microscale model of the skin in order to increase our understanding of pressure-induced ischemia through microvascular collapse. We use a space-filling fractal generation algorithm to create the vasculature trees. Our algorithm follows from previous work on fractal generating algorithms in two dimensions that were designed to generate the Purkinje fiber networks of the human heart (Costabal et al. 2016). Other, similar work includes two-dimensional fractals of blood vessel geometries (Vankan et al. 1997) and space-filling fractal tree generation in three dimensions to model the airways (Tawhai et al. 2000).
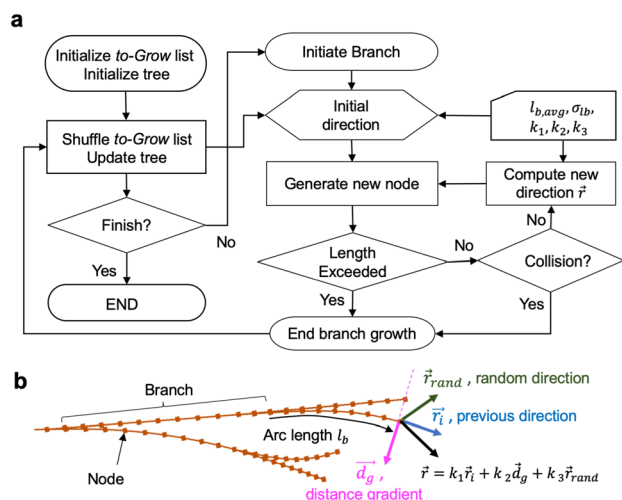
To create the fractal network of the microvasculature, we first choose a progenitor node and a random growth direction. We then initiate a branch creation loop. The flowchart of the algorithm is shown in Fig. 2a. Once the first branch

Fig. 2 Fractal generation algorithm. **a** Flowchart defining the growth of the tree and also the subroutine for a single branch. Once a branch is initialized, it grows by a node at each iteration. The branch growth terminates if the branch collides with another branch or if the branch arc length exceeds a threshold length drawn from a normal distribution of lengths controlled by parameters $l_{b,avg}, \sigma_{lb}$. **b** At each iteration, the branch grows in the direction $\vec{r}$ determined from the sum of three contributions: (i) previous growth direction $\vec{r}_i$, (ii) negative of the closest distance vector to any other branch in the tree $\vec{d}_g$, and (iii) random contribution $\vec{r}_{rand}$. The parameters k_1, k_2, k_3 control the new direction $\vec{r}$

attains a required length and reaches the *End branch growth* condition in Fig. 2a, we stop growing this branch, bifurcate the tree, and start the growth of two new branches from the terminal node of the original branch. This loop continues for a required number of generations which is decided a priori. While initially there is one branch to grow, this number increases exponentially with more generations of the tree. All the branches that need to grow at a particular instant during the execution of the algorithm are stored in a *To-Grow* list. There are several instances in the algorithm in which randomness is incorporated. One of those instances is the order in which branches are grown. The *To-Grow* list is shuffled every time a branch reaches the *End branch growth* condition in Fig. 2a, before the growth of the next branch.

Following initialization of a branch, the algorithm enters a loop that grows the branch in the direction $\vec{r}$ at each new iteration $i + 1$. The vector $\vec{r}$ is chosen so that the tree is space filling and random (Ijiri et al. 2008; Costabal et al. 2016). To achieve these features, $\vec{r}$ is computed at each iteration by summing three contributions with different weights: (i) The branch tends to continue growing in the previous direction $\vec{r}_i$; (ii) the branches are biased to grow in the direction $\vec{d}_g$, the unit vector aligned with the closest distance vector between the current branch and all other branches, (iii) there is a random contribution $\vec{r}_{rand}$ (Fig. 2b).

The termination of the branch growth algorithm in Fig. 2a also includes a random input. As the branch grows, we compute the branch length value l_b, which measures the arc length of a branch. The final branch length needed in Fig. 2a to determine whether or not to end the growth of the current branch is assumed to be a random variable, normally distributed, with a mean branch length $l_{b,avg}$ and a standard deviation σ_{lb}. The parameters $l_{b,avg}$ and σ_{lb} may be independent for each branch. To match the skin microvasculature, for example, we decrease the mean branch length $l_{b,avg}$ for successive generations of the tree (Cevc and Vierl 2007). Branch growth can be terminated even if the branch has not achieved the required length, if the distance between the current branch and any other branch in the tree is less than a predetermined tolerance ($\varepsilon = 1\,\mu m$). In this case, the growth of a branch is terminated due to collision with another branch, and no new branches emerge from this terminal node.

The parameters of the algorithm can be modified to make sure that the fractals replicate the properties of the skin vasculature (Braverman 1989; Cevc and Vierl 2007; Davis and Lawler 1958). Skin is characterized by blood vessels with lengths on the order of $100\,\mu m$ for the initial, lower levels of the tree. From these initial vessels, there are 8–10 bifurcations along the thickness direction, each leading to a decrease in length of around 40%, such that the top plexus is composed of vessels with lengths of about $10\,\mu m$. In this model, we do not resolve the vessels

into the level of single capillaries. This range of blood vessel diameter is limited in part by the complexity of the finite element simulation. Moreover, we expect that collapse of the larger 10–20 μ-m-diameter vessels will be a major factor in ischemia, although further refinements into even smaller scales can be achieved at the expense of greater computational cost. Our modeling assumption is supported by observations in microangiograms of small vessels in nailfolds subjected to compressive strain (Choi et al. 2014). In these experiments, blood flow was cut off even at the top plexus, i.e., before reaching the capillary loops connecting venules and arterioles. It remains to elucidate whether the presence of smaller capillaries with diameters in the range [3, 10] μm has a substantial effect on the overall deformation patterns of the microvascular tree.

The final volume fraction of vasculature is in the order of $\phi_0 \sim 0.5\%$ (Meglinski and Matcher 2002; Nilsson et al. 1980; Lister et al. 2012). Additionally, vessel diameters reported in Cevc and Vierl (2007) indicate that the vessels in the middle and upper generations of the tree are in the range 10–30 μm.

In summary, the fractal growth algorithm is controlled by five parameters. The length of the different branches is governed by the parameters $l_{b,avg}$ and σ_{lb}. Following the discussion of the previous paragraph, we set $l_{b,avg} = 100$ μm for the originating branch and reduce this value by 40% at each bifurcation (Cevc and Vierl 2007; Braverman 1989). We set $\sigma_{lb} = 0.01 l_{b,avg}$ and keep it constant during the entire execution of the algorithm. The remaining three parameters controlling the algorithm are k_1, k_2 and k_3, which appear in the expression for $\vec{r}$ (see Fig. 2b). The values of the parameters used here are $k_1 = 1$, $k_2 = 0.1$, $k_3 = 0.05$. These parameters yield trees with the features of the skin vasculature outlined above (Cevc and Vierl 2007; Braverman 1989; Braverman et al. 1990; Davis and Lawler 1958).

2.2 Finite element model of the representative volume element

From a fractal tree generated with the algorithm described in the previous section, we generate a RVE of the skin in several steps. Figure 3a shows a typical fractal tree representing the skin vasculature. First, we convert this tree to a three-dimensional CAD model as shown in Fig. 3b using the software FreeCAD (Riegel and Werner 2001–2018). More specifically, since the fractal tree
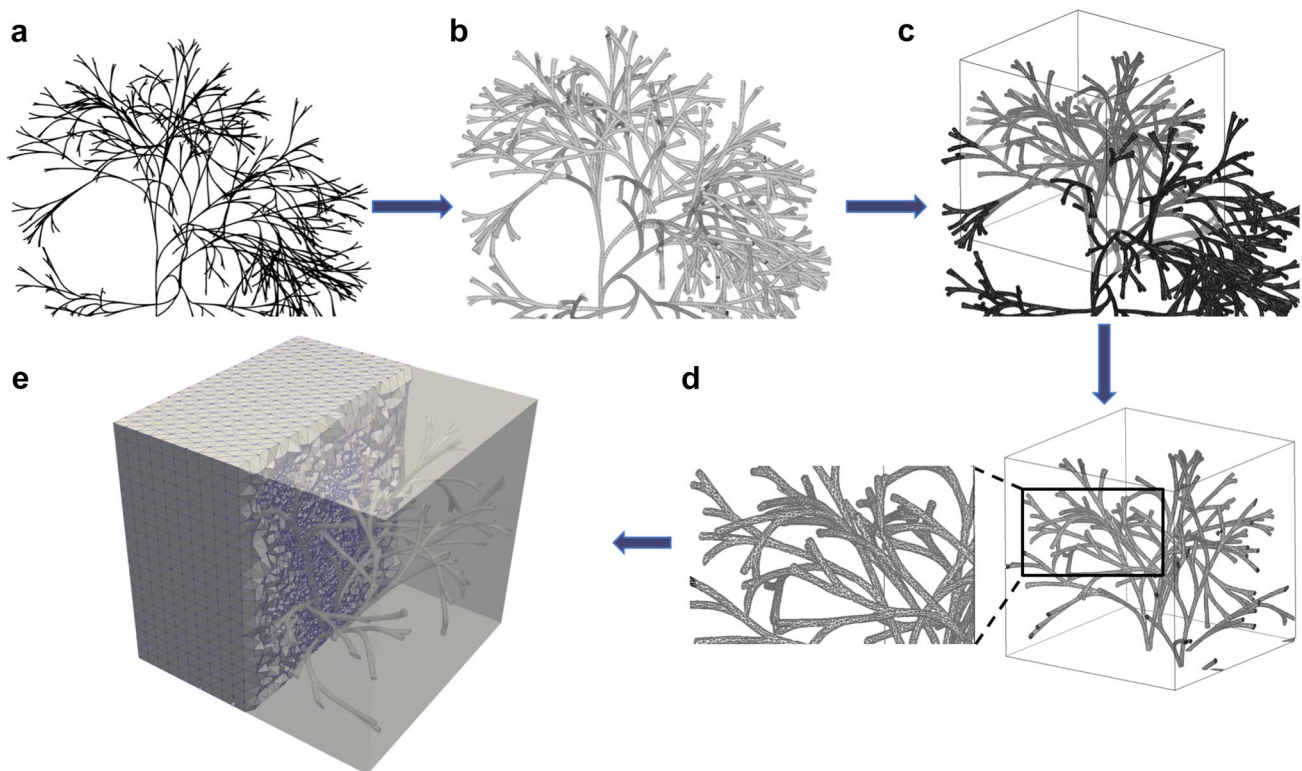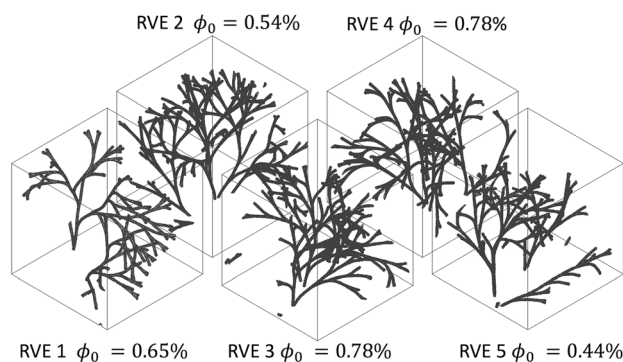

Fig. 3 Generation of the RVE model. **a** A tree of the microvasculature generated with our fractal algorithm. **b** Solid cylinders are generated for each branch of the tree and then combined into a single solid. **c** We fit a smooth, closed surface to the solid tree using the Poisson reconstruction algorithm and embed the surface into a solid 1 mm³ cube. **d** We subtract the tree from the cube to generate the RVE. **e** The geometry is meshed with tetrahedral elements. For the tree shown, the mesh consists of 203,697 nodes and 1,208,437 elements

defines the centerline of the blood vessels, we execute a script in FreeCAD to sweep cylinders along each branch. The diameter of these cylinders is set to 20 μm. A Boolean union operation combines each of these cylinders into a single solid structure. Then, in an additional step, we generate a closed and smooth surface to the union of all cylinders using the Poisson surface reconstruction algorithm (Kazhdan and Hoppe 2013). We are not interested in the vasculature itself, but instead on the tissue surrounding the vasculature. Thus, we embed the surface reconstruction of the vessel tree into a solid 1 mm³ cube and perform a Boolean subtraction operation (Fig. 3c). The final result from these processing steps is shown in Fig. 3d. Note that the portion of the tree outside the 1 mm³ is discarded in this process. The inset showcases the detail of the vessel structures. The CAD model is exported as an IGES file and imported into the commercial finite element software package Abaqus Standard for meshing and analysis. A typical mesh used in our simulations is shown in Fig. 3e. The mesh shown consists of 203,697 nodes and 1,208,437 tetrahedral elements.

Due to the inherent randomness incorporated into the fractal generation algorithm, we can generate different vascular geometries even from the same initial conditions and parameter set. Five such geometries are shown in Fig. 4. The volume fraction of the vascular trees is indicated alongside each geometry in Fig. 4. The range of volume fractions across the different RVEs is well in agreement with the typically observed blood volume fraction in human skin (Cevc and Vierl 2007; Meglinski and Matcher 2002).

We discretize the RVE geometries using linear tetrahedral elements (C3D4) in Abaqus. Contact constraints are introduced along the inner walls of the microvasculature using the elastic, surface to surface contact feature in Abaqus. These contacts are necessary to prevent unrealistic deformations such as interpenetration due to the displacement and deformation of the vessel walls.
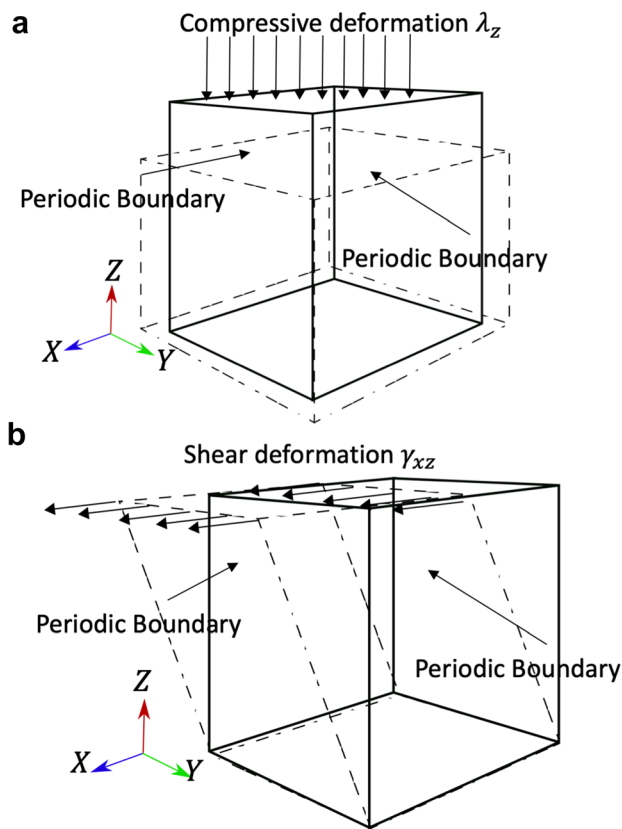
Skin is commonly modeled as a hyperelastic material, and a number of strain energy functions have been proposed to model skin's mechanical response (Benítez and Montáns 2017; Limbert 2017). There are material models that consider the presence of a collagen fiber network in the material of interest, some of which have been applied to skin (Lanir 1983; Limbert 2014; Rausch 2017; Gasser et al. 2005). In this study, however, we opt for an isotropic Neo-Hookean description, similar to previous studies (Buganza-Tepole et al. 2014). While skin does exhibit anisotropy, with a dispersion parameter for the fiber network in the range $\kappa \in [0.1306, 0.1675]$ with $\kappa = 0$ denoting perfect anisotropy and $\kappa = 0.333$ perfect isotropy (Annaidh et al. 2012), the preliminary analysis shown here does not include the effect of a fiber family. Thus, we use the strain energy density function of the form

$$\Psi = C_{10}(\bar{I}_1 - 3) + \frac{1}{D_1}(J - 1)^2, \tag{1}$$

where $C_{10} = \mu_0/2$, μ_0 is the shear modulus, $\bar{I}_1$ is the first invariant of the isochoric part of the right Cauchy–Green deformation tensor, $J = \det(\mathbf{F})$ is the volume ratio or Jacobian, with $\mathbf{F}$ the deformation gradient, and $D_1 = 1/K$, where K is the bulk modulus. The notation C_{10} and D_1 is used to match the Abaqus notation, but in the rest of the manuscript we refer only to shear and bulk modulus values. From previous experimental studies on skin (Iivarinen et al. 2011), the estimated baseline parameters for the dermis are $\mu_0 = 75$ kPa and $K = 350$ kPa.

Normal compression and shear deformation of human skin are the most important deformation modes implicated in pressure ulcer formation (Mak et al. 2010). Therefore, we perform simulations directly controlling compressive and shear strains on the RVE. To obtain the response of skin under these types of deformation, we enforce periodic boundary conditions on all outer surfaces except for the top and bottom surfaces. While we do not explicitly model blood flow, we apply tractions due to blood pressure of 20 mmHg at inner walls of the vascular RVE inclusion (Shore 2000). For the compression simulation, the displacement is specified at the top surface of the RVE while the bottom surface is constrained in the z-direction, resulting in the compressive stretch λ_z (Fig. 5a). For the shear simulation, the bottom is again held fixed while Dirichlet boundary conditions are applied to the top surface in lateral direction, leading to a shear strain γ_{xz} (Fig. 5b). In theory, both shear and compression may occur simultaneously (Maklebust and Sieggreen 2001); we explore this type of coupled loading in Appendix.

The primary variable of interest obtained from the simulations is the volume fraction occupied by the deforming blood vessels, ϕ. This volume fraction is related to the total blood volume within the skin. Thus, we are interested in

Fig. 4 Five different RVEs resulting from performing the same fractal generating algorithm and post-processing steps. The variation in the trees is due to the incorporation of random inputs in the fractal algorithm. The volume fraction for the RVEs, ϕ_0, is within the physiological values for skin
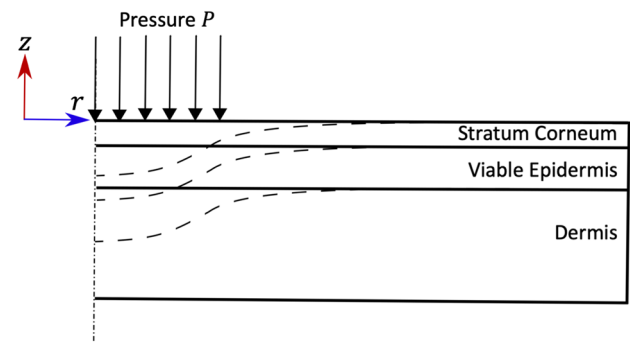
a

b

Fig. 5 RVE simulations. **a** We apply a normal compressive strain λ_z by controlling the relative displacement between the top and bottom surfaces of the RVE, and the lateral surfaces satisfy periodic boundary conditions. **b** Shear is applied to the RVE by controlling the x-displacement of the top surface with respect to the bottom surface, while maintaining periodic boundary conditions on the lateral surfaces of the RVE

Fig. 6 Tissue model. We consider an axisymmetric domain with outer diameter of 5 cm. Three skin layers are considered: stratum corneum, viable epidermis, and dermis. The bottom of the domain is constrained, whereas a normal pressure load is applied at the center of the domain $r \in [0, 5]\,\mathrm{mm}$

how this variable changes as the RVE deforms. Since the initial blood volume fraction, ϕ_0, is different for each of the RVEs in Fig. 4, we compute a normalized change in volume fraction: $\hat{\phi} = \phi/\phi_0$. This normalization also enables us to calculate an average response as a function of deformation, regardless of the specific value of ϕ_0. Thus, from a set of simulations for different values of λ_z and γ_{xz}, we seek functions $f_1 : \lambda_z \rightarrow \hat{\phi}$ and $f_2 : \gamma \rightarrow \hat{\phi}$ that describe the average response of the normalized volume fraction of blood under compression and shear.

2.3 Oxygen diffusion at the tissue scale

One of the key goals of the proposed simulation framework is to link the deformation of the skin to tissue hypoxia through the prediction of microvascular collapse. We thus introduce a tissue-level model of skin ischemia mechanics. For the tissue-level simulations, we use *Comsol Multiphysics*, a commercial finite element solver. Figure 6 shows an

axisymmetric domain of skin tissue. We model three different layers according to the skin anatomy. The top layer is the stratum corneum, with a thickness of 0.02 mm. The second layer is the viable epidermis, with a thickness of 0.1 mm. The bottom layer is the dermis tissue, and in this case the initial thickness is $t_0 = 1.38$ mm (Benítez and Montáns 2017; Bruls et al. 1984; Holbrook and Odland 1974). The domain considered has a radius of $r_o = 25$ mm. The domain is discretized using quadratic quadrilateral serendipity elements.

Indentation experiments have previously demonstrated that the viable epidermis and the stratum corneum have distinct mechanical properties from that of the dermis (Groves et al. 2013). We model all three skin layers as a Neo-Hookean material, but with different shear moduli. For the dermis, in line with the RVE simulations, we use $\mu = 75$ kPa and $K = 350$ kPa (Iivarinen et al. 2011). The viable epidermis is approximately 3–10 times stiffer under indentation compared to the dermis (Geerligs et al. 2011). We thus assign $\mu = 200$ kPa for the epidermis. The stratum corneum has a similar stiffness under indentation to that of the viable epidermis (Geerligs et al. 2011). Hence, we also use $\mu = 200$ kPa for the stratum corneum.

In the tissue-level model, we solve for the oxygen concentration distribution with a homogenized diffusion equation. We also solve the linear momentum balance equation to obtain the tissue deformation as the tissue is subjected to relevant loading conditions. Since the domain considered is axisymmetric, the fixed boundary conditions are $u_r = 0$ at $r = 0$ mm, and $u_z = 0$ at $z = -1.5$ mm. The top of the domain has a compressive pressure applied along $r \in [0, 5]$ mm. In the oxygen diffusion partial differential equation, the primary variable is the transcutaneous oxygen partial pressure P_{O_2}, which indirectly measures the oxygen concentration in the skin. Partial oxygen pressure is also the most common directly observed quantity reported in previous experimental studies related to skin hypoxia (Manorama et al. 2010; Colin

and Saumet 1996; Peirce et al. 2000). The reaction diffusion equation solved for the oxygen partial pressure is

$$\alpha \frac{\partial P_{O_2}}{\partial t} + \nabla \cdot \mathbf{q} = s_{P_{O_2}}, \qquad (2)$$

where $\mathbf{q} = -D\alpha\nabla P_{O_2}$ is the flux assumed to follow Fickian diffusion with diffusivity $D\alpha$, and $s_{P_{O_2}}$ is the source term. Note that no advective transport of oxygen is considered. The diffusivity of oxygen is given by the diffusion coefficient D and the oxygen solubility α. Here, $D = 1.5 \times 10^{-3}$ mm^2/s, and $\alpha = 3 \times 10^{-5}$ mm^{3}O$_2$/mm^3 mmHg in the germinal layer of epidermis and in the dermal tissue (Wang 2005). For the stratum corneum, these parameters are assumed to be an order of magnitude less to account for low water content in the cells: $D = 1.5 \times 10^{-4}$ mm^2/s and $\alpha = 3 \times 10^{-6}$ mm^{3}O$_2$/mm^3 mmHg (Wang 2005; Grossmann 1982). The physiological oxygen source rate is assumed to be $s_0 = 0.8 \times 10^{-5}$ s^{-1}, and no production or consumption term is assumed in the stratum corneum due to the absence of living cells. The baseline oxygen source term is manually calibrated such that the contours match physiological reported conditions (Wang et al. 2003).

The key coupling term between deformation and ischemia is the source term $s_{P_{O_2}}$. It is reasonable to consider that the total blood volume in the skin is proportional to the oxygen available in the tissue scale. Thus, we assume that the source term is proportional to the normalized volume fraction. This now enables us to link the deformation simulations of the RVEs to the tissue-scale hypoxia model. At any point in the domain, we can retrieve the amount of normal compression λ_z and shear γ and evaluate the homogenized functions $f_1 \equiv \hat{\phi}_1$ and $f_2 \equiv \hat{\phi}_2$ as defined in the previous section. The modified source term is then computed based on our prediction of the deformed volume fraction: $s_{P_{O_2}} = \hat{\phi}s_0$. The vessel tree extends all the way to the bottom interface. Thus, in line with the scaling of the source term inside the domain, the bottom surface is subject to an essential boundary condition with a similar scaling $P_{O_2} = 65\hat{\phi}$ mmHg. The top boundary also has a Dirichlet boundary condition, in this case to atmospheric oxygen concentration, except in the region where the compressive load is applied, which is set to $P_{O_2} = 0$ mmHg. The boundary $r = 25$ mm satisfies no-flux boundary condition. Only steady-state simulations are shown in Results section; however, transient analysis is also possible.

3 Results

3.1 Compression and shear of the RVEs

We first subject the RVEs shown in Fig. 4 to compressive strains and focus on the deformation of the microvasculature.

Figure 7a shows the contours of the normal component of the strain tensor, E_{zz}, over the outer boundary of the domain. The columns from left to right show the sequential compression of the tissue as the top surface of the RVE is displaced to produce the average stretch λ_z. Although only a single RVE is shown, the behavior is similar in all five RVEs. The overall strain contours on the boundary of the domain are fairly homogeneous. The second row in Fig. 7a shows multiple cross sections of the domain. In the cross sections, it is apparent that even though the E_{zz} contours are constant over large portions of the domain, there are localized strain concentrations close to the vessels, which is indicative of the large deformations that the vessels undergo compared to the surrounding material.

Isolating the deformed vessel geometry reveals that some vessels collapse at moderately low RVE stretch λ_z. This is further illustrated in detail in Fig. 8a, b. The reference configuration of one of the RVEs is shown in Fig. 8a together with the corresponding detail of the vessel surface. Figure 8b then shows the same RVE after a compression of $\lambda_z = 0.8$. We highlight that with these levels of overall stretch, some of the vessels collapse, as seen in the inset in Fig. 8b.

The application of the normal stretch is accompanied by in plane deformation, allowable based on the periodic boundary conditions. In combination, the deformation of the lateral surfaces of the RVE and the normal stretch λ_z lead to a change in the volume occupied by the RVE. By extracting the deformed vessel geometry (Fig. 8b), we compute the volume change associated with the microvasculature alone. For the RVE shown in Fig. 7a the initial volume of the vasculature is 0.00782 mm^3, and the final volume is 0.00373 mm^3. A more detailed analysis of the change in normalized volume fraction is presented later in this section.

The result from a shear deformation simulation for one of our RVEs is depicted in Fig. 7b. Analogous to the compression simulation, applying an average shear γ_{xz} to the entire RVE by prescribing the displacement of the top and bottom surfaces and periodic boundary conditions on the lateral surfaces results in overall homogeneous strain contours as seen in the sequence of snapshots of Fig. 7b. Similar to the compression case, upon closer inspection, it becomes apparent that there are localized regions of higher shear strain, E_{xz}, near the vessels (Fig. 7b). However, in contrast to the compression case, when the RVE is subjected to simple shear, the vessels do not undergo complete closure even under large values of γ_{xz}. Isolating the vessel geometry and magnifying the detail of the deformed tree illustrate the shape changes that are typically seen for the vessels. The cross section of the vasculature becomes elongated but the vessels do not collapse (Fig. 8c).

We focus on the vasculature volume fraction as the homogenized variable of interest because this variable is linked to the total blood volume in the skin tissue. It is
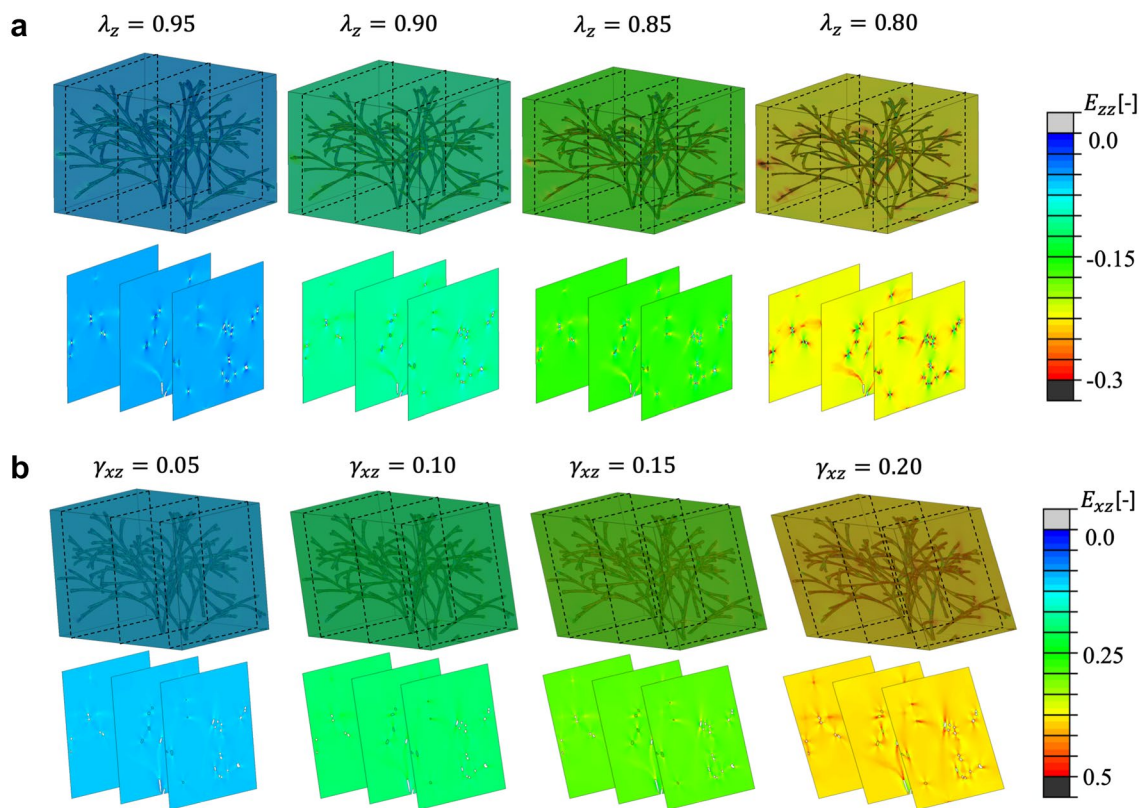
Fig. 7 Compression and shear of a RVE. **a** Sequence of snapshots of the RVE compression simulation. The contours of the normal component of the Green Lagrange strain, E_{zz} are homogeneous over most of the domain, but cross sections reveal higher strains surrounding the blood vessels. **b** Snapshots of an RVE subjected to increasing shear γ_{xz}. Once again, the E_{xz} of the Green Lagrange strain tensor appears constant over the domain, with cross sections showing that there are high strains surrounding the vascular tree
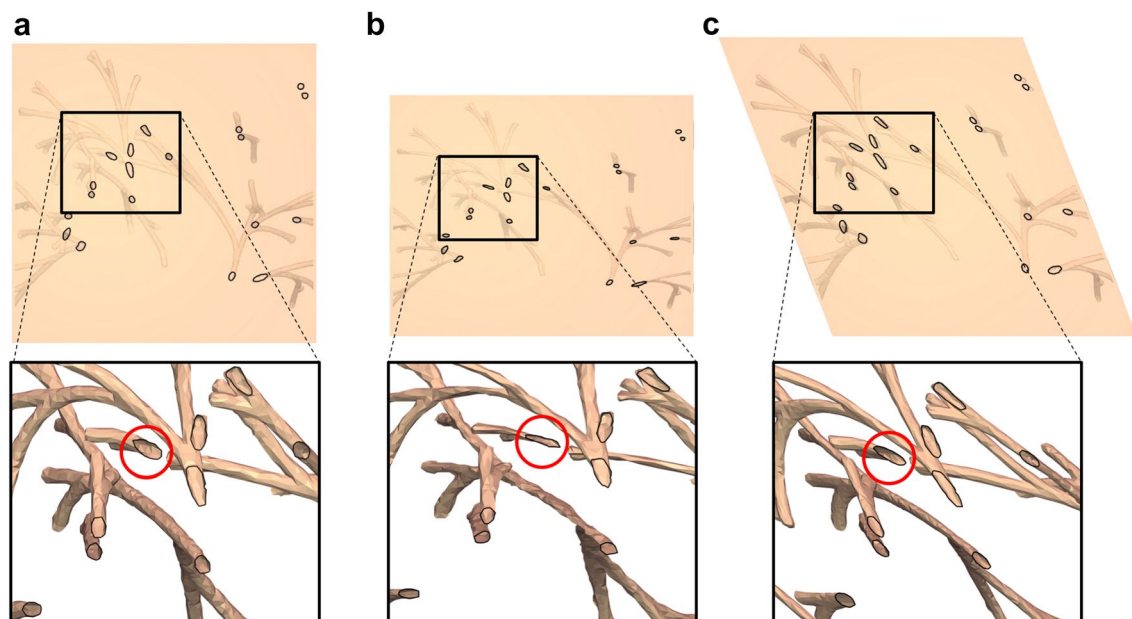
Fig. 8 Extraction of the vasculature geometry as the RVE deforms. **a** The reference configuration of one of the RVEs and the corresponding detail of the vasculature tree. **b** The result of one compression simulation up to λ_z. Isolating the deformed vessel geometry, we compute the change in volume fraction as well as identify the collapse of some of the vessels. **c** Deformed tree due to RVE shear γ_{xz}. The inset shows that even at high shear the vessels deform but do not fully collapse
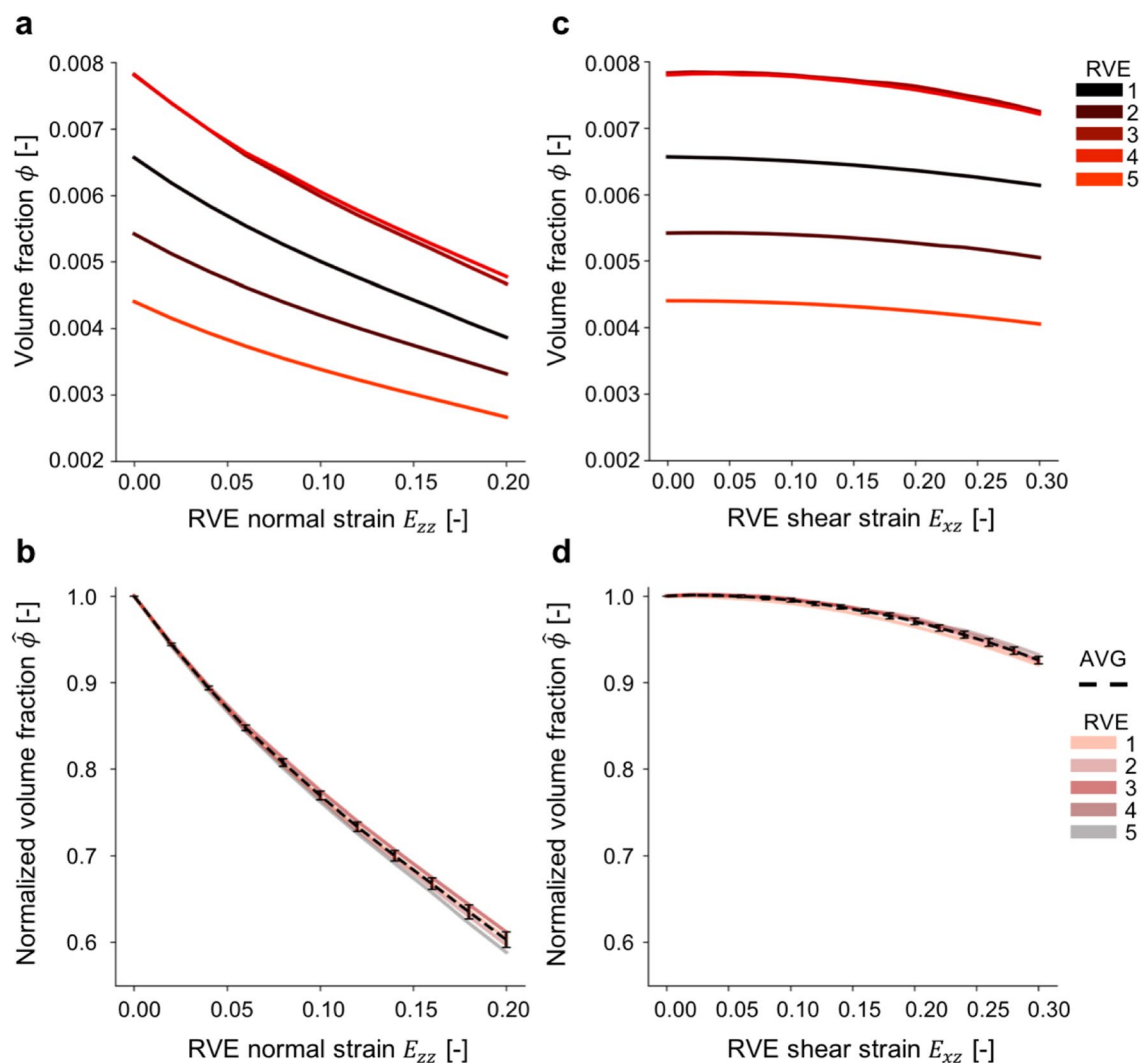
Fig. 9 Change in volume fraction of the vasculature tree in response to compression and shear of the RVE. **a** Absolute change in the volume fraction of the vascular tree when the RVE is subjected to compression. Different curves indicate RVEs with different volume fractions due to the randomness incorporated in the tree generation. **b** Normalized volume fraction curves collapse into a single response

for all five RVEs considered, revealing that a 20% compressive strain leads to more than 40% reduction in normalized blood volume fraction. **c** Shear causes a small change in volume fraction of the different RVEs. **d** Normalized volume fraction curves for the RVE shear simulations also collapse into a single response with very little deviation between the different RVEs

also reasonable to assume that the amount of blood contained within the distributed vascular network at any time is proportional to the source term for the oxygen diffusion model, as explained in Methods section. Then, a reduction in volume fraction of the vascular tree indicates that the total blood volume in the tissue decreases and causes a corresponding decrease in the oxygen availability. The volume fraction of the blood vessels is calculated on the deformed vasculature surfaces isolated from the deformed RVEs as shown in Fig. 8.

Figure 9a shows the change in volume fraction of blood vessels due to applied compressive stretch λ_z. Since each RVE geometry in Fig. 4 has a different volume fraction in

the reference configuration due to the randomness incorporated into the fractal generation algorithm, the change in volume fraction is not directly comparable across RVEs. To obtain a single function $f := \hat{\phi}_1(\lambda_z)$ describing the average RVE response, we normalize the volume fraction values by the initial volume fraction of each RVE. The results for the normalized volume fraction are shown in Fig. 9b. Interestingly, this normalization collapses the volume fraction change of all the RVEs into a single response, with very little deviation among the different curves. From Fig. 9b, it is easier to observe the degree to which the normal stretch causes reduction in blood volume. Application of 20% compressive strain leads to a drop of about 40% of the normalized volume

fraction. If we consider the fact that some blood vessels may have completely collapsed at intermediate points in the tree, occluding any blood flow to the vessels further along in the tree, as reported before (Choi et al. 2014), the actual blood volume may be even less than our initial estimate. Thus, our estimate of the blood volume fraction could be seen as a conservative indicator of blood perfusion.

As noted before, the applied shear strain on the RVE causes deformation of the vessels, but rarely does it lead to collapse. Therefore, the change in volume fraction for the shear simulations is smaller compared to the compression cases. Figure 9c shows the change in volume fraction with increasing shear for the five different RVEs. Similar to before, we compute the corresponding normalized change in volume fraction. Upon normalization, the curves collapse into a single response depicted in Fig. 9d, just as it was the case for the compression simulations. We note that the shear-induced normalized volume fraction change is only about 10% for shear strains of 30%. This indicates that compression may be a more relevant mode of deformation to cause ischemia compared to simple shear.

In the clinical setting, a combination of shear and compression is likely (Maklebust and Sieggreen 2001). Accordingly, we performed additional simulations with this combined loading mode, applying compression first, followed by shear. The results are shown in Appendix. Interestingly, the same trends are observed: Initial compression substantially reduces the volume fraction of blood vessels, with the subsequent shear decreasing the volume only slightly.

To further elucidate the role of individual vessel geometry and orientation on the collapse trends, we performed simulations of individual inclusions with different orientations and volume fractions. The results are also shown in Appendix. These simulations indicate that for noninteracting vessels, the orientation of the vessel is the single most important factor leading to collapse. The trends are independent of volume fraction, and thus, we expect that smaller capillaries, although not captured in our simulation of the vascular tree, will also show similar trends. The statistics of the vessel orientation in our five RVEs are also reported in Appendix.

The RVEs span the thickness of the dermis, showing a rapidly changing vascular tree and raising the question of whether the change in volume fraction shows a dependence on the z-coordinate. An analysis of the change in volume fraction at different depths along the RVE thickness is shown in Appendix and reveals that the reduction in normalized volume fraction does not show a strong dependence on the z-coordinate.

We use the average of the curves plotted in Fig. 9b, d to approximate the function linking vessel volume change to the oxygen source term in the diffusion model. With no prior knowledge of the shape of these curves, we decided to fit them with cubic polynomials

$$\hat{\phi}_1 = -14.061(1 - \lambda_z)^3 + 7.5901(1 - \lambda_z)^2 - 2.926(1 - \lambda_z) + 0.992, \quad (3)$$

with an standard error of 0.0008454 and a R^2 value of 0.9999. For the shear deformation, we have the fit

$$\hat{\phi}_2 = -0.055\gamma_{xz}^3 - 0.9492\gamma_{xz}^2 + 0.0419\gamma_{xz} + 1.0003, \quad (4)$$

which has an standard error of 0.00288 and a R^2 value of 0.9999. Due to the substantially smaller contribution of shear to blood volume change, and considering situations at the tissue scale in which skin is mostly under a large compressive strain but small shear, we ignore the contribution from $\hat{\phi}_2$ in the tissue simulations and consider only the function $\hat{\phi}_1$ to link both scales.

3.2 Hypoxia at the tissue level

We first ensure that the tissue-scale model of oxygen diffusion matches the physiological steady-state profiles of oxygen concentration. To set this baseline condition, we use the tissue-scale model described in Methods section but we do not apply any loading at the top surface. Setting the oxygen source term to $s_{P_{O_2}} = s_0 = 0.8 \times 10^{-5}$ s^{-1} in the dermis, we obtain the oxygen concentration profile shown in Fig. 10a, top. This contour matches the expected in vivo profiles reported experimentally and from other numerical modeling efforts (Stücker et al. 2002; Wang 2005; Grossmann 1982). The outer layer of the skin is in contact with the atmosphere and is thus exposed to an oxygen partial pressure of $P_{O_2} = 160$ mmHg. The region on the top surface of the epidermis where the pressure load is applied is not in contact with the atmosphere, and the boundary condition for this part of the top boundary is $P_{O_2} = 0$ mmHg.

The oxygen contours in the top panel of Fig. 10a show that, in the physiological setting, the viable epidermis receives some oxygen from the atmosphere, but there is a sharp gradient and the oxygen partial pressure drops to about $P_{O_2} = 40$ mmHg at the interface between the viable epidermis and the dermis. The dermis also shows a gradient of oxygen concentration in the physiological state. However, since the dermis domain has the source term representing the oxygen supplied by the blood, the gradient is only significant at the top of the dermis, a continuation of the gradient from the epidermis, but the concentration quickly settles to a value of $P_{O_2} = 60$ mmHg in most of the dermis domain.

When pressure is applied at the top, the tissue deforms substantially, see Fig. 10a. To couple this deformation to the oxygen source term, we use the function $s_{P_{O_2}} = \hat{\phi}_1(\lambda_z)s_0$. Note that the $\hat{\phi}_1$ function is defined at every location of the domain and hence will introduce a spatial heterogeneity in
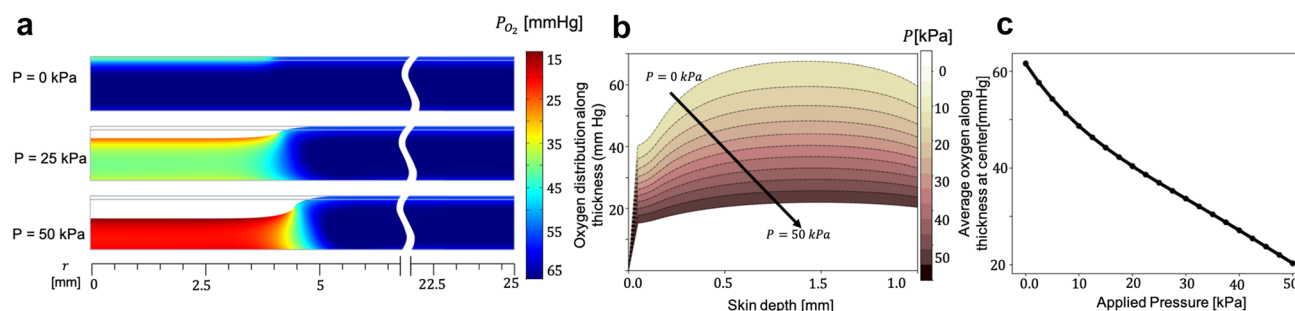
Fig. 10 Tissue-level simulations predict patterns of tissue hypoxia from applied pressure at the top surface of the skin. **a** Contours of partial oxygen pressure P_{O2} for different loading conditions. When no load is applied, the oxygen profile shows a sharp gradient across the stratum corneum and the epidermis, but the partial oxygen pressure achieves a near constant value for the dermis due to the presence of a source term in this domain. As pressure is applied, the tissue is compressed. We link the normal strain to the oxygen source term through our homogenized vessel volume fraction variable from the RVE model. As a result, we predict patterns of tissue hypoxia. **b** Plots of oxygen concentration at the centerline of the domain for different pressures. The drop in partial oxygen pressure is most significant in the dermis. **c** Integrating the curves in **b** summarizes the effect of applied pressure on oxygen concentration. As pressure increases up to 120 kPa, out model predicts a drop of more than 60% in oxygen partial pressure

the model even though the underlying response $\hat{\phi}_1$ comes from the set of simulations with the multiple RVEs under a range of normal strains. Figure 10a shows the representative contours of the oxygen concentration when the compressive pressure at the top surface is 60 and 120 kPa. Increasing the pressure leads to greater hypoxia, as expected. For the 60 kPa case, we see that the central region, right under the part of the boundary where pressure is applied, shows a reduction in partial oxygen pressure of about 30%. The gradient is not constant through the thickness but rather it shows an hourglass shape. Nevertheless, the hypoxic region is mostly confined to the column of tissue under compression. This hourglass shape can be expected from diffusion of oxygen from the surrounding tissue into the compressed tissue. At 120 kPa, the oxygen in the central region is further diminished. In conclusion, applied normal pressure leads to a significant reduction in oxygen concentration, despite the surrounding tissue being well perfused.

The plot in Fig. 10b illustrates the variation of the oxygen partial pressure along the thickness direction $z \in [0, -1.5]$ mm at the centerline of the domain $r = 0$ mm. The point at the epidermal surface at the top of the domain, where the pressure boundary condition is applied, is not in contact with the atmosphere and hence $P_{O_2} = 0$ mmHg at this point. Oxygen concentration increases through the epidermis and in the interface between stratum corneum and viable epidermis, $z = -0.02$ mm, partial pressure of oxygen is 40 mmHg in the absence of loading, but it drops to 15 mmHg as pressure is applied. The most extreme changes in the oxygen profile occur in the dermis. In the middle of the dermis, at $z = -0.75$ mm for instance, the oxygen partial pressure goes from 65 to 18 mmHg as the pressure load is increased to 120 kPa.

The plot in Fig. 10c shows the integral of the oxygen profile along the centerline as a function of applied pressure at the top surface. Namely, Fig. 10c results from integrating the curves in Fig. 10b. The relationship is nonlinear, with a very steep decrease initially compared to at higher pressures. This averaging over the entire thickness better illustrates the significance of our results: The oxygen partial pressure drops from 60 to 20 mmHg as the applied pressure increases to 120 kPa.

3.3 Effect of skin anatomy and mechanical properties on pressure-induced hypoxia

Pressure ulcers are more common in the older adult population. However, the exact way in which aging increases the susceptibility to pressure ulcers is not fully understood. There are indications that biological changes in inflammation with age affect pressure ulcer progression (Moor et al. 2014). There are also behavioral factors involved in the increased susceptibility to pressure ulcers with aging (Allman et al. 1995). Here, we are interested in factors that may play a role in the susceptibility to ischemia, the initiation step of pressure ulcers. In particular, changes in skin anatomy and mechanical properties with age have been reported (Luebberding et al. 2014; Leveque et al. 1984), but whether or not these changes could affect susceptibility to ischemia remains unknown. We therefore decided to use our multiscale model to increase our understanding of how changes in skin anatomy and mechanical properties can influence the pressure-induced hypoxia profiles. Our parameter study focuses on the shear modulus μ and the thickness t. The value of the shear modulus used up to this point, $\mu_0 = 75$ kPa is representative of adult skin dermis (Iivarinen et al. 2011). The thickness value used thus far, $t_0 = 1.5$ mm,
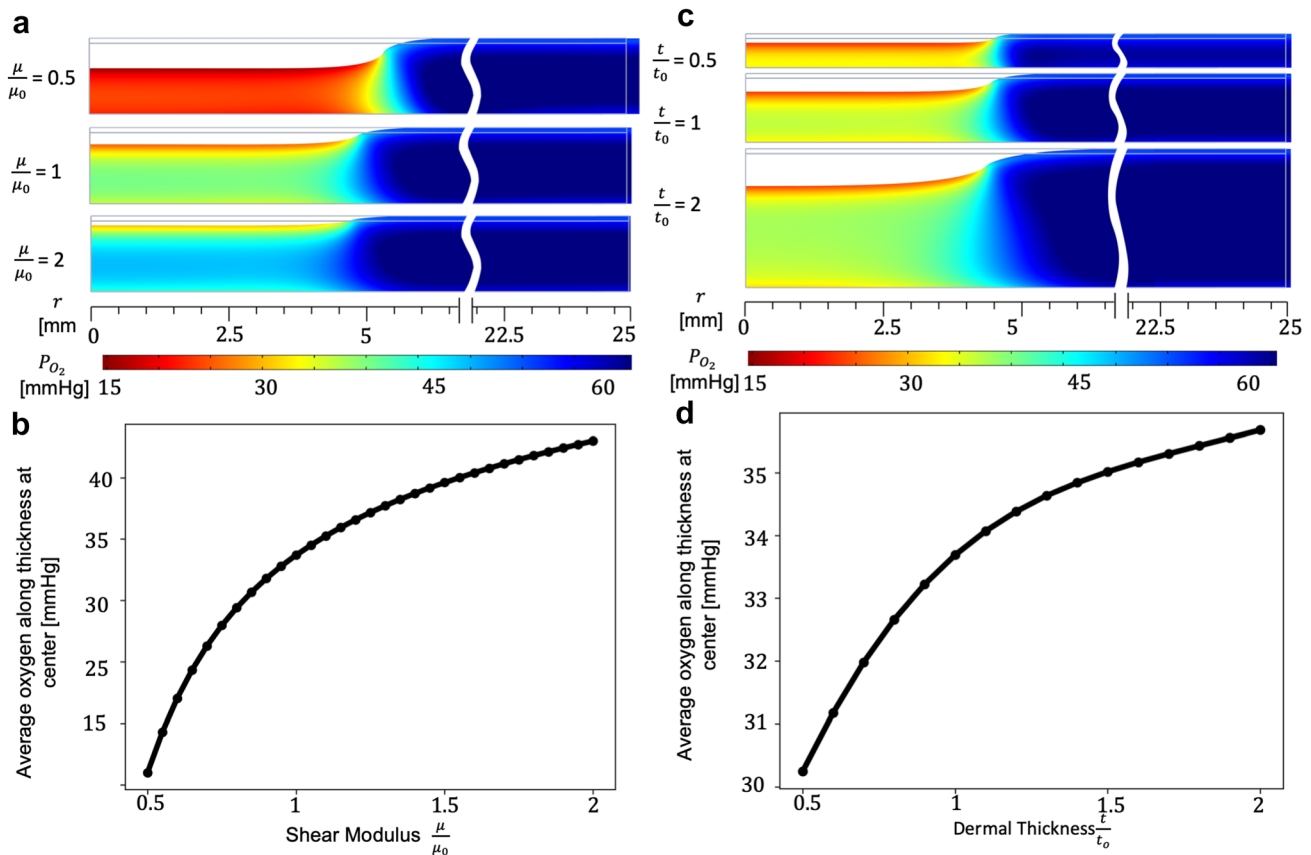
Fig. 11 Parametric study showing the effect of changing the tissue stiffness μ and thickness t on the profiles of tissue hypoxia under applied pressure. **a** A weaker skin, $\mu < \mu_0$ shows a higher degree of hypoxia but a similar contour to those observed with the baseline parameters. A stiffer skin, $\mu > \mu_0$ has the opposite effect on the contour values. **b** Averaging the oxygen concentration at the center and plotting the result against the normalized changes in the shear modulus, we see that the tissue model of oxygen diffusion is very sensitive

to a decrease in μ. **c** Changing the dermis thickness leads also to a change in hypoxia values under applied load. As thickness increases, hypoxic regions become more pronounced at the top and bottom of the dermis. Increasing thickness leads to less severe hypoxia compared to a decrease in thickness. **d** Integrating the oxygen profile at the center as thickness changes reveals that the amount of hypoxia is less sensitive to a variation in thickness compared to the sensitivity of the oxygen profiles to tissue's shear modulus

is also representative of adult skin (Benítez and Montáns 2017). We apply a pressure of 60 kPa at the top surface of the skin, analogous to previous simulations, but we change the thickness over the range $t/t_0 \in [0.5, 2]$, and the shear modulus over the range $\mu/\mu_0 \in [0.5, 2]$.

Figure 11 summarizes the results of our parametric study. Changes in the mechanical properties of skin have a marked influence on the oxygen concentration profiles. Qualitatively, the contours look similar to those in Fig. 10a. Hypoxia is mostly confined to the column of tissue right below the portion of the top boundary where pressure is applied. The hypoxic region continues to show the hourglass shape encountered in Fig. 10a. As the shear modulus increases, however, it can be noticed that the hypoxic regions are not evenly distributed but occur mostly at the upper and lower ends of the dermis. Even though the oxygen profiles are of similar shape to those seen in Fig. 10a, the values change significantly with a

change in shear modulus compared to the baseline. As could be expected, weaker skin, i.e., $\mu < \mu_0$, leads to higher strains and therefore more severe tissue hypoxia. Stiffer skin leads, as intuited, to less hypoxic conditions. The plot in Fig. 11b shows the integral of the oxygen concentration over the centerline of the domain. Interestingly, this curve is nonlinear, showing that variation from our initial estimate μ_0 toward a stiffer value only has a moderate effect on the oxygen partial pressure, whereas decreasing μ_0 from the nominal value yields a more drastic change in oxygen partial pressure.

From the parametric study concerning t, we see that an increase in thickness is beneficial; i.e., it protects the tissue against hypoxia. The opposite also holds, and thinning of the dermis leads to a decrease in the oxygen contours with applied pressure. The contours continue to be qualitative similar compared to those in Fig. 10a. Yet, as the thickness increases, the hypoxic regions are not constant through the

entire thickness, but are rather concentrated at the top and bottom of the dermis. Figure 11d then shows the integral of the oxygen profile along the centerline. Here, it can be seen that reducing the thickness with respect to the nominal value has a marked effect on the oxygen concentration, whereas increasing the thickness shows a moderate increase in the partial oxygen pressure at the center of the domain. Regardless, it should also be noted that while the sensitivity of the oxygen curves is similar for both parametric studies, it is the variation in the shear modulus that produces the most significant changes in the oxygen contours.

4 Discussion

In this paper, we present a multiscale model to link vasculature collapse at the microscopic scale with oxygen diffusion at the tissue scale. Our current understanding of pressure ulcers points to pressure-driven ischemia as the key factor in ulcer initiation (Coleman et al. 2014). However, our knowledge of this process is limited due to the difficulty in imaging the microvasculature in vivo in relevant clinical settings (Timar-Banu et al. 2001; Choi et al. 2014). Therefore, to get a better understanding of how applied pressure can lead to ischemia and, subsequently, to hypoxia, and to use this knowledge in the prevention and treatment of pressure ulcers, we need predictive models. Here, we show the first numerical investigation of how applied pressure can lead to deformation and collapse of realistic three-dimensional microvascular trees of the skin and how the collapse of blood vessels at the microscopic scale can be linked to hypoxia at the tissue level. While a careful calibration of our model is still needed, the geometries and material properties we use are based on reports of the vascular anatomy and mechanical behavior of skin available in the literature (Cevc and Vierl 2007; Iivarinen et al. 2011). Therefore, we are confident that our investigation is properly contextualized in the current knowledge and that it paves the way for future experiments to calibrate and test the predictions of our model. This work also sets a foundation for more sophisticated models that can address unsettled questions of how nonbehavioral changes with aging can lead to a higher susceptibility to pressure ulcers in the older adult population.

4.1 Microvascular collapse depends on vessel orientation distribution and is driven by compression and not shear

Previous work on ex vivo imaging of the vasculature allowed us to generate realistic RVEs representative of the skin (Cevc

and Vierl 2007; Braverman 1989; Braverman et al. 1990). We then used these geometries to study how realistic deformations of the skin can lead to microvascular collapse and subsequent tissue hypoxia. Our work is not without limitations. In the RVE simulations, we ignored a detailed coupling of the solid matrix with the fluid flow inside of the blood vessels. A clear direction for future research is to include the fluid domain and solve the nontrivial coupled fluid–structure interaction problem as discussed in Causin and Malgaroli (2017) and Casquero et al. (2016). We also limited our attention to vessels in the $[10, 20]\,\mu m$ diameter range, but resolution of capillaries, at least in a lumped manner, could improve the model.

Compression and shear simulations of the RVE led to insightful results. A key observation based on our simulations is that even though we generated random RVEs, each with a unique vessel tree and slightly different volume fraction in the reference configuration, all the curves of vessel volume change against RVE strains collapsed into a single normalized volume fraction response. Additional analysis of individual inclusions as well as statistics of the orientation of the vessels in our RVEs indicates that vessel orientation distribution is the single most important factor leading to vessel collapse for noninteracting vessels. It remains to explore this phenomenon further in order to uncover the microscale characteristics that dictate the trends seen, especially for denser networks that include smaller vessels and possible mechanical interaction among different branches in the tree.

Another key result of our simulations is that pure shear does not result in a significant reduction of blood vessel volume fraction. This observation might be a consequence of the distinctive geometric features of the vascular tree as mentioned above. Our result raises some questions about the importance of simple shear for hypoxia. The role of shear deformations on tissue damage has been discussed before (Mak et al. 2010). Additional experimental work is needed to validate our predictions that compression of the skin in the thickness direction is the primary mechanism of pressure-driven ischemia. Moreover, here we focus mostly on compression or simple shear of the RVE. Combined loading by applying first compression followed by shear showed similar trends to the simulations with compression or shear alone. Yet, a more realistic setup that we are currently pursuing is to subject the RVEs to arbitrary deformations and use data-driven modeling techniques to learn the corresponding microvasculature deformation response (Teichert et al. 2018). One additional limitation in our modeling approach is the choice of constitutive model of the skin. Here, we use a Neo-Hookean strain energy function, but future work will focus on more detailed constitutive models including the effect of anisotropy.

4.2 At the tissue scale, applied pressure leads to nonlinear and spatial variation in hypoxia contours

Our multiscale model reveals that the relationship between applied pressure and hypoxia at the tissue level is highly nonlinear. From the results of the RVE deformation, we first see that normal strains of 20% cause more than a 40% drop in the normalized volume fraction of the vasculature. This first relationship, at the RVE level, is only slightly nonlinear as can be seen in Fig. 9b. However, connecting these results to a tissue-level model of oxygen diffusion, we are then able to connect applied pressure at the skin outer surface to the oxygen concentration through the skin thickness. The corresponding plot (Fig. 10c) shows that the coupling of the different physical phenomena across scales increases the nonlinearity and sensitivity of the variable of interest, the oxygen concentration in the skin. In fact, the results indicate that the application of a 120 kPa load, which is within the range of physiological loads (Verver et al. 2004; Makhsous et al. 2007; Drummond et al. 1982; Allen et al. 1993; Oomens et al. 2003), produces a drop of more than 50% in oxygen compared to the physiological regime. This level of hypoxia has been shown to hinder the growth rate of native skin cells and collagen deposition in in vitro experiments (Horikoshi et al. 1986; Gottrup 2004). A more thorough calibration is of course needed. For instance, we assumed that the oxygen source term is linearly related to the normalized volume fraction of blood in the dermis. This assumption has the limitation that the transport across the vessel membrane is not considered. The model can be improved by accounting for blood flow and transport between the blood circulating in the microvasculature and the surrounding tissue (Causin et al. 2016). Additionally, there are other features of tissue perfusion that we ignore, such as the active control of the vasculature to regulate blood flow, especially in response to externally applied pressure (Pan et al. 2018). This type of endeavor is beyond the scope of this manuscript. Nevertheless, even with the simplified connection between microvasculature deformation and oxygen supply, our simulations yield results consistent with the current understanding of pressure-driven ischemia and ulcer formation.

One of the primary motivations for developing the current model is that it enables the simulation of pressure-driven hypoxia for arbitrary domains. Here, we show a relatively simple domain for the tissue-level simulations. However, the problem can be easily extended to more realistic settings. With our axisymmetric domain, we show that the oxygen concentration contours have a characteristic geometry. The region where hypoxia is more evident is right underneath the surface of the epidermis where the load is applied. The oxygen contours are not constant through the thickness but rather show an hourglass-shaped hypoxic region for the baseline thickness and material properties considered. Future work will focus on more realistic clinical scenarios.

4.3 Changes in skin anatomy and mechanics with aging may contribute to increased susceptibility to pressure ulcers

Finally, one more advantage of the tissue-level model is the ability to investigate in silico how changes in skin anatomy and mechanical behavior can be linked to corresponding changes in pressure-driven hypoxia. Recent studies in mice show that skin's strain–stress response shifts toward larger strains, i.e., the tissue is more compliant at moderate stresses (Lynch et al. 2017). Here, we show that the oxygen contours are very sensitive to a reduction in skin stiffness, possibly explaining one factor involved in the greater susceptibility to pressure ulcer initiation with age. We also know that skin changes in thickness as we grow older, becoming thinner (Daly and Odland 1979). Incorporating this knowledge into our model, we find that the effect of dermis thinning with respect to our baseline does not result in a dramatic change in the oxygen concentration profile under applied pressure compared to the change in stiffness. Interestingly, a recent study in mice suggests that older but obese mice may be at less risk to ulcer initiation due to the increased thickness of their skin (Nguyen-Tu et al. 2013). In line with this hypothesis, we predict that the pressure-driven ischemic response is sensitive to an increase in thickness with respect to our baseline.

One limitation in our approach is that the RVEs were generated based on reports of the vascular anatomy of adults (Cevc and Vierl 2007; Braverman 1989). Further work is needed to incorporate changes in vasculature anatomy with aging (Bentov and Reed 2015). For example, it has been reported that the vasculature in older adults is less dense compared to a younger population (Li et al. 2006). Our study shows that, for the range of volume fractions considered, the initial volume fraction has no influence on the normalized volume fraction changes under applied RVE deformation. However, more work is needed to know whether this trend remains true for networks of different density. It is also needed to characterize the baseline level of oxygen perfusion in the older adult population and compare it to the adult population (Ogrin et al. 2005). Other changes in vasculature anatomy with age, and not just volume fraction, may also contribute to a different microvasculature deformation pattern.

5 Conclusion

In conclusion, we present a multiscale model that predicts hypoxia contours in skin at the tissue level based on a microscale model of vascular collapse. We use skin-specific geometries, constitutive parameters, and microvascular characteristics reported in the literature. The model predicts oxygen concentration contours indicative of tissue hypoxia when moderate levels of pressure are applied at the skin outer surface. The predictions are in good agreement with existing knowledge of pressure-driven ischemia. Our model enabled us to explore for the first time how changes in skin with aging might affect the increased susceptibility to pressure-induced ischemia in the older adult population. Therefore, we expect that future work will allow us to further calibrate and validate the model, and lead to the development of better prevention and treatment tools for pressure ulcers that incorporate age-specific changes in skin anatomy and mechanical properties.

References

Allen V, Ryan D, Murray A (1993) Repeatability of subject/bed interface pressure measurements. J Biomed Eng 15:329–332

Allman RM, Goode PS, Patrick MM, Burst N, Bartolucci AA (1995) Pressure ulcer risk factors among hospitalized patients with activity limitation. JAMA 273:865–870

Annaidh AN, Bruyere K, Destrade M, Gilchrist MD, Maurini C, Otténio M, Saccomandi G (2012) Automated estimation of collagen fibre dispersion in the dermis and its contribution to the anisotropic behaviour of skin. Ann Biomed Eng 40:1666–1678

Ashcroft GS, Herrick SE, Tarnuzzer RW, Horan MA, Schultz GS, Ferguson MW (1997) Human ageing impairs injury-induced in vivo expression of tissue inhibitor of matrix metalloproteinases (TIMP)-1 and-2 proteins and mRNA. J Pathol J Pathol Soc G B Irel 183:169–176

Benítez JM, Montáns FJ (2017) The mechanical behavior of skin: structures and models for the finite element analysis. Comput Struct 190:75–107

Bentov I, Reed MJ (2015) The effect of aging on the cutaneous microvasculature. Microvasc Res 100:25–31

Braverman IM (1989) Ultrastructure and organization of the cutaneous microvasculature in normal and pathologic states. J Investig Dermatol 93:S2–S9

Braverman IM, Keh A, Goldminz D (1990) Correlation of laser doppler wave patterns with underlying microvascular anatomy. J Investig Dermatol 95:283–286

Bruls WA, Slaper H, van Der Leun JC, Berrens L (1984) Transmission of human epidermis and stratum corneum as a function of thickness in the ultraviolet and visible wavelengths. Photochem Photobiol 40:485–494

Buganza-Tepole A, Steinberg JP, Kuhl E, Gosain AK (2014) Application of finite element modeling to optimize flap design with tissue expansion. Plast Reconstr Surg 134:785

Casquero H, Liu L, Bona-Casas C, Zhang Y, Gomez H (2016) A hybrid variational-collocation immersed method for fluid-structure interaction using unstructured t-splines. Int J Numer Methods Eng 105:855–880

Causin P, Malgaroli F (2017) Mathematical modeling of local perfusion in large distensible microvascular networks. Comput Methods Appl Mech Eng 323:303–329

Causin P, Guidoboni G, Malgaroli F, Sacco R, Harris A (2016) Blood flow mechanics and oxygen transport and delivery in the retinal microcirculation: multiscale mathematical modeling and numerical simulation. Biomech Model Mechanobiol 15:525–542

Cevc G, Vierl U (2007) Spatial distribution of cutaneous microvasculature and local drug clearance after drug application on the skin. J Controll Release 118:18–26

Choi WJ, Wang H, Wang RK (2014) Optical coherence tomography microangiography for monitoring the response of vascular perfusion to external pressure on human skin tissue. J Biomed Opt 19:056003

Coleman S, Nixon J, Keen J, Wilson L, McGinnis E, Dealey C, Stubbs N, Farrin A, Dowding D, Schols JM et al (2014) A new pressure ulcer conceptual framework. J Adv Nurs 70:2222–2234

Colin D, Saumet J (1996) Influence of external pressure on transcutaneous oxygen tension and laser doppler flowmetry on sacral skin. Clin Physiol 16:61–72

Costabal FS, Hurtado DE, Kuhl E (2016) Generating Purkinje networks in the human heart. J Biomech 49:2455–2465

Crichton ML, Donose BC, Chen X, Raphael AP, Huang H, Kendall MA (2011) The viscoelastic, hyperelastic and scale dependent behaviour of freshly excised individual skin layers. Biomaterials 32:4670–4681

Daly CH, Odland GF (1979) Age-related changes in the mechanical properties of human skin. J Investig Dermatol 73(1):84–87

Davis MJ, Lawler JC (1958) The capillary circulation of the skin: some normal and pathological findings. AMA Arch Dermatol 77:690–703

Dealey C, Brindle CT, Black J, Alves P, Santamaria N, Call E, Clark M (2015) Challenges in pressure ulcer prevention. Int Wound J 12:309–312

Demarré L, Van Lancker A, Van Hecke A, Verhaeghe S, Grypdonck M, Lemey J, Annemans L, Beeckman D (2015) The cost of prevention and treatment of pressure ulcers: a systematic review. Int J Nurs Stud 52:1754–1774

Drummond DS, Narechania RG, Rosenthal AN, Breed AL, Lange TA, Drummond DK (1982) A study of pressure distributions measured during balanced and unbalanced sitting. J Bone Jt Surg Am 64(7):1034–1039

Gasser TC, Ogden RW, Holzapfel GA (2005) Hyperelastic modelling of arterial layers with distributed collagen fibre orientations. J R Soc Interface 3:15–35

Gawlitta D, Oomens CW, Bader DL, Baaijens FP, Bouten CV (2007) Temporal differences in the influence of ischemic factors and deformation on the metabolism of engineered skeletal muscle. J Appl Physiol 103:464–473

Geerligs M, Van Breemen L, Peters G, Ackermans P, Baaijens F, Oomens C (2011) In vitro indentation to determine the mechanical properties of epidermis. J Biomech 44:1176–1181

Gerhardt L-C, Schmidt J, Sanz-Herrera J, Baaijens F, Ansari T, Peters G, Oomens C (2012) A novel method for visualising and quantifying through-plane skin layer deformations. J Mech Behav Biomed Mater 14:199–207

Goldberger AL, Bhargava V, West BJ, Mandell AJ (1985) On a mechanism of cardiac electrical stability. The fractal hypothesis. Biophys J 48:525–528

Gottrup F (2004) Oxygen in wound healing and infection. World J Surg 28:312–315

Gould DJ, Vadakkan TJ, Poché RA, Dickinson ME (2011) Multifractal and lacunarity analysis of microvascular morphology and remodeling. Microcirculation 18:136–151

Grossmann U (1982) Simulation of combined transfer of oxygen and heat through the skin using a capillary-loop model. Math Biosci 61:205–236

Groves RB, Coulman SA, Birchall JC, Evans SL (2013) An anisotropic, hyperelastic model for skin: experimental measurements, finite element modelling and identification of parameters for human and murine skin. J Mech Behav Biomed Mater 18:167–180

Hahn HK, Georg M, Peitgen HO (2005) Fractal aspects of three-dimensional vascular constructive optimization. In: Losa GA (ed) Fractals in biology and medicine. Springer, pp 55–66

Hendriks F, Brokken D, Oomens C, Bader D, Baaijens F (2006) The relative contributions of different skin layers to the mechanical behavior of human skin in vivo using suction experiments. Med Eng Phys 28:259–266

Holbrook KA, Odland GF (1974) Regional differences in the thickness (cell layers) of the human stratum corneum: an ultrastructural analysis. J Investig Dermatol 62:415–422

Horikoshi T, Balin AK, Carter DM (1986) Effect of oxygen on the growth of human epidermal keratinocytes. J Investig Dermatol 86(4):424–427

Iivarinen JT, Korhonen RK, Julkunen P, Jurvelin JS (2011) Experimental and computational analysis of soft tissue stiffness in forearm using a manual indentation device. Med Eng Phys 33:1245–1253

Ijiri T, Ashihara T, Yamaguchi T, Takayama K, Igarashi T, Shimada T, Namba T, Haraguchi R, Nakazawa K (2008) A procedural method for modeling the purkinje fibers of the heart. J Physiol Sci 58:481–486

Jor JW, Parker MD, Taberner AJ, Nash MP, Nielsen PM (2013) Computational and experimental characterization of skin mechanics: identifying current challenges and future directions. Wiley Interdiscip Rev Syst Biol Med 5:539–556

Kazhdan M, Hoppe H (2013) Screened poisson surface reconstruction. ACM Trans Graph (TOG) 32:29

Kosiak M (1961) Etiology of decubitus ulcers. Arch Phys Med Rehabil 42:19

Krueger N, Luebberding S, Oltmer M, Streker M, Kerscher M (2011) Age-related changes in skin mechanical properties: a quantitative evaluation of 120 female subjects. Skin Res Technol 17:141–148

Kumaraswamy N, Khatam H, Reece GP, Fingeret MC, Markey MK, Ravi-Chandar K (2017) Mechanical response of human female breast skin under uniaxial stretching. J Mech Behav Biomed Mater 74:164–175

Lanir Y (1983) Constitutive equations for fibrous connective tissues. J Biomech 16:1–12

Lee T, Turin SY, Gosain AK, Tepole AB (2018) Multi-view stereo in the operating room allows prediction of healing complications in a patient-specific model of reconstructive surgery. J Biomech 74:202–206

Lee T, Gosain AK, Bilionis I, Tepole AB (2019) Predicting the effect of aging and defect size on the stress profiles of skin from advancement, rotation and transposition flap surgeries. J Mech Phys Solids 125:572–590

Leveque J, Corcuff P, Rigal Jd, Agache P (1984) In vivo studies of the evolution of physical properties of the human skin with age. Int J Dermatol 23:322–329

Li L, Mac-Mary S, Sainthillier J-M, Nouveau S, De Lacharriere O, Humbert P (2006) Age-related changes of the cutaneous microcirculation in vivo. Gerontology 52:142–153

Liao F, Burns S, Jan Y-K (2013) Skin blood flow dynamics and its role in pressure ulcers. J Tissue Viability 22:25–36

Limbert G (2014) State-of-the-art constitutive models of skin biomechanics. In: Querleux B (ed) Computational Biophysics of the Skin. Taylor and Francis, pp 95–131

Limbert G (2017) Mathematical and computational modelling of skin biophysics: a review. Proc R Soc A 473:20170257

Linder-Ganz E, Gefen A (2007) The effects of pressure and shear on capillary closure in the microstructure of skeletal muscles. Ann Biomed Eng 35:2095–2107

Lister T, Wright PA, Chappell PH (2012) Optical properties of human skin. J Biomed Opt 17:090901

Liu X, Cleary J, German G (2016) The global mechanical properties and multi-scale failure mechanics of heterogeneous human stratum corneum. Acta Biomater 43:78–87

Loerakker S, Stekelenburg A, Strijkers G, Rijpkema J, Baaijens F, Bader D, Nicolay K, Oomens C (2010) Temporal effects of mechanical loading on deformation-induced damage in skeletal muscle tissue. Ann Biomed Eng 38:2577–2587

Loerakker S, Manders E, Strijkers GJ, Nicolay K, Baaijens FP, Bader DL, Oomens CW (2011) The effects of deformation, ischemia, and reperfusion on the development of muscle damage during prolonged loading. J Appl Physiol 111:1168–1177

Lokshin O, Lanir Y (2009) Viscoelasticity and preconditioning of rat skin under uniaxial stretch: microstructural constitutive characterization. J Biomech Eng 131:031009

Luebberding S, Krueger N, Kerscher M (2014) Mechanical properties of human skin in vivo: a comparative evaluation in 300 men and women. Skin Res Technol 20:127–135

Lyder CH, Ayello EA (2008) Pressure ulcers: a patient safety issue. Agency for Healthcare Research and Quality (US), Rockville

Lynch B, Bonod-Bidaud C, Ducourthial G, Affagard J-S, Bancelin S, Psilodimitrakopoulos S, Ruggiero F, Allain J-M, Schanne-Klein M-C (2017) How aging impacts skin biomechanics: a multiscale study in mice. Sci Rep 7:13750

Mak AF, Zhang M, Tam EW (2010) Biomechanics of pressure ulcer in body tissues interacting with external forces during locomotion. Annu Rev Biomed Eng 12:29–53

Makhsous M, Lim D, Hendrix R, Bankard J, Rymer WZ, Lin F (2007) Finite element analysis for evaluation of pressure ulcer on the buttock: development and validation. IEEE Trans Neural Syst Rehabil Eng 15:517–525

Maklebust J, Sieggreen M (2001) Pressure ulcers: guidelines for prevention and management. Lippincott Williams & Wilkins, Philadelphia

Mandelbrot BB (1985) Self-affine fractals and fractal dimension. Phys Scr 32:257

Manorama AA, Baek S, Vorro J, Sikorskii A, Bush TR (2010) Blood perfusion and transcutaneous oxygen level characterizations in human skin with changes in normal and shear loads implications for pressure ulcer formation. Clin Biomech 25:823–828

Meglinski IV, Matcher SJ (2002) Quantitative assessment of skin layers absorption and skin reflectance spectra simulation in the visible and near-infrared spectral regions. Physiol Meas 23:741

Mitchell N, Sifakis E et al (2015) Gridiron: an interactive authoring and cognitive training foundation for reconstructive plastic surgery procedures. ACM Trans Graph (TOG) 34:43

Moor AN, Tummel E, Prather JL, Jung M, Lopez JJ, Connors S, Gould LJ (2014) Consequences of age on ischemic wound healing in rats: altered antioxidant activity and delayed wound closure. Age 36:733–748

Müller B, Elrod J, Pensalfini M, Hopf R, Distler O, Schiestl C, Mazza E (2018) A novel ultra-light suction device for mechanical characterization of skin. PloS ONE 13:e0201440

Nguyen-Tu M-S, Begey A-L, Decorps J, Boizot J, Sommer P, Fromy B, Sigaudo-Roussel D (2013) Skin microvascular response to pressure load in obese mice. Microvasc Res 90:138–143

Nilsson GE, Tenland T, Oberg PA (1980) Evaluation of a laser Doppler flowmeter for measurement of tissue blood flow. IEEE Trans Biomed Eng 27(10):597–604

Ogrin R, Darzins P, Khalil Z (2005) Age-related changes in microvascular blood flow and transcutaneous oxygen tension under basal and stimulated conditions. J Gerontol Ser A Biol Sci Med Sci 60:200–206

Oomens C, Van Campen D, Grootenboer H (1987) A mixture approach to the mechanics of skin. J Biomech 20:877–885

Oomens CWJ, Bressers O, Bosboom E, Bouten C, Bader D (2003) Can loaded interface characteristics influence strain distributions in muscle adjacent to bony prominences? Comput Methods Biomech Biomed Eng 6:171–180

Pailler-Mattei C, Bec S, Zahouani H (2008) In vivo measurements of the elastic mechanical properties of human skin by indentation tests. Med Eng Physics 30:599–606

Pan W, Drost JP, Roccabianca S, Baek S, Bush TR (2018) A potential tool for the study of venous ulcers: blood flow responses to load. J Biomech Eng 140:031009

Park CJ, Clark SG, Lichtensteiger CA, Jamison RD, Johnson AJW (2009) Accelerated wound closure of pressure ulcers in aged mice by chitosan scaffolds with and without bFGF. Acta Biomater 5:1926–1936

Peirce SM, Skalak TC, Rodeheaver GT (2000) Ischemia-reperfusion injury in chronic pressure ulcer formation: a skin model in the rat. Wound Repair Regen 8:68–76

Rausch MK, Humphrey JD (2017) A computational model of the biochemomechanics of an evolving occlusive thrombus. J Elast 129:125–144

Riegel J, Werner M, van Havre Y (2001–2018) FreeCAD (version 0.17.13541). http://www.freecadweb.org/. Accessed Mar 2019

Sadler Z, Scott J, Drost J, Chen S, Roccabianca S, Bush TR (2018) Initial estimation of the in vivo material properties of the seated human buttocks and thighs. Int J Non Linear Mech 107:77–85

Shilo M, Gefen A (2012) Identification of capillary blood pressure levels at which capillary collapse is likely in a tissue subjected to large compressive and shear deformations. Comput Methods Biomech Biomed Eng 15:59–71

Shimizu H (2007) Shimizu's textbook of dermatology. Hokkaido University, Sapporo

Shore AC (2000) Capillaroscopy and the measurement of capillary pressure. Br J Clin Pharmacol 50:501–513

Sree VD, Rausch MK, Tepole AB (2019) Towards understanding pressure ulcer formation: coupling an inflammation regulatory network to a tissue scale finite element model. Mech Res Commun. https://doi.org/10.1016/j.mechrescom.2019.05.003

Stücker M, Struk A, Altmeyer P, Herde M, Baumgärtl H, Lübbers DW (2002) The cutaneous uptake of atmospheric oxygen contributes significantly to the oxygen supply of human dermis and epidermis. J Physiol 538:985–994

Tawhai MH, Pullan A, Hunter P (2000) Generation of an anatomically based three-dimensional model of the conducting airways. Ann Biomed Eng 28:793–802

Teichert G, Marquis E, Garikipati K (2018) Machine learning materials physics: algorithm predicts precipitate morphology in an alternative to phase field dynamics. arXiv preprint arXiv:1806.00503

Tepole AB (2017) Computational systems mechanobiology of wound healing. Comput Methods Appl Mech Eng 314:46–70

Timar-Banu O, Beauregard H, Tousignant J, Lassonde M, Harris P, Viau G, Vachon L, Levy E, Abribat T (2001) Development of noninvasive and quantitative methodologies for the assessment of chronic ulcers and scars in humans. Wound Repair Regen 9:123–132

Tonge TK, Atlan LS, Voo LM, Nguyen TD (2013) Full-field bulge test for planar anisotropic tissues: part I—experimental methods applied to human skin tissue. Acta Biomater 9:5913–5925

Vankan W, Huyghe J, Janssen J, Huson A, Hacking W, Schreiner W (1997) Finite element analysis of blood flow through biological tissue. Int J Eng Sci 35:375–385

Verver M, Van Hoof J, Oomens C, Wismans J, Baaijens F (2004) A finite element model of the human buttocks for prediction of seat pressure distributions. Comput Methods Biomech Biomed Eng 7:193–203

Wang W (2005) Oxygen partial pressure in outer layers of skin: simulation using three-dimensional multilayered models. Microcirculation 12:195–207

Wang W, Winlove C, Michel C (2003) Oxygen partial pressure in outer layers of skin of human finger nail folds. J Physiol 549:855–863

Weickenmeier J, Jabareen M, Mazza E (2015) Suction based mechanical characterization of superficial facial soft tissues. J Biomech 48:4279–4286